

## Grid methods for cold molecules: Determination of photoassociation line shapes and rate constants

S. Kallush,<sup>1,2</sup> R. Kosloff,<sup>2</sup> and F. Masnou-Seeuws<sup>1</sup>

<sup>1</sup>*Laboratoire Aimé Cotton, CNRS, Bâtiment 505, Campus d'Orsay, 91405 Orsay Cedex, France*

<sup>2</sup>*The Fritz Haber Research Center, The Hebrew University of Jerusalem, Jerusalem 91904, Israel*

(Received 2 January 2007; published 17 April 2007)

A description of photoassociation by cw laser is formulated in the framework of grid methods. The Hamiltonian describing one or several bound states coupled to a multiple of continuum manifolds via a radiative field is written in the energy representation and diagonalized. The generality of the treatment allows us to compute accurately and efficiently physical properties such as nonlinear high-intensity energy shifts, line shapes, and photoassociation rates both for isolated and nonisolated resonances. Application is given to sodium photoassociation in the experimental conditions of McKenzie *et al.* [Phys. Rev. Lett. **88**, 090403 (2002)]. Inverted regions for the dependency of the rate vs the intensity and nonsymmetric line shapes are predicted to occur above the saturation limit. Comparison with the model of Bohn and Julienne [Phys. Rev. A **60**, 414 (1999)] is discussed.

DOI: [10.1103/PhysRevA.75.043404](https://doi.org/10.1103/PhysRevA.75.043404)

PACS number(s): 34.50.Rk, 33.80.Ps, 42.50.Hz

### I. INTRODUCTION

Many experimental groups are presently working on the formation of ultracold molecules and molecular quantum gases. A very efficient scheme is the photoassociation reaction, where two colliding atoms absorb a photon to make a molecule [1]; moreover, ultracold photoassociation spectroscopy [2] is capable of providing deep insight into the properties of long range molecules, cold atomic collisions, or pair correlations in a condensate. Theoretical two-body scattering models have been developed to compute the photoassociation rates [3–7], in the framework of a perturbative treatment, adapted to situations where low-intensity cw lasers are employed and many-body effects are negligible. A linear variation of the photoassociation rate as a function of intensity is then predicted. In the work of Bohn and Julienne [6], which develops a semianalytic theory yielding laser-induced energy shifts and line broadening, the departure from this linear behavior is described, the saturation limit at larger laser intensities being evaluated. In a condensate, the two-body model should fail and Javanainen and Mackie [8] have developed a many-body theory which predicts a saturation limit occurring at lower intensities and attributed to rogue photodissociation. The search for saturation effects has stimulated several experiments. Measurement, by McKenzie *et al.* [9], of the photoassociation rate in a sodium condensate as a function of laser intensity has shown a linear behavior in the intensity range considered, in agreement with the two-body Bohn and Julienne estimation, and in contrast with the prediction of Javanainen and Mackie. For a quantum degenerate lithium atomic gas, measurement [10] of the intensity dependence of the photoassociation rate has verified both the large value of this rate (at a temperature  $T=600$  nK) and the two-body saturation effect at intensities  $I \geq 30$  W/cm<sup>2</sup>. The agreement with theory is considered as reasonable within the present experimental accuracy: The higher value of the measured saturation limit, and the oscillations in the experimental rate in the 30–80 W/cm<sup>2</sup> intensity range should be confirmed by measurements with a smaller error bar. For a

nondegenerate gas of cesium atoms, at a temperature of 40  $\mu$ K, within an optical dipole trap, saturation limit is reached for intensities above 100 W/cm<sup>2</sup> [11], and the experimental values then lay around the theoretical curve: It is not clear whether such oscillations are due to uncertainties or should be attributed to a physical effect.

Recently Naidon and Masnou-Seeuws [12] have developed a time-dependent many-body theory of photoassociation in an atomic Bose-Einstein condensate, showing that several physical effects depend on pair correlations. They show that the two existing models for the description of such correlations [13,14] differ in their predictions of the photoassociation line shapes at large intensities. Precise measurements of the variation of the line shapes as a function of cw laser intensity should therefore give insight into the optimal description of many-body effects.

The aim of the present paper is to anticipate such measurements by revisiting the theoretical treatment of photoassociation line shapes, taking advantage of the efficiency of grid methods [15–18] for the numerical description of cold collisions and long range molecules, particularly in cases where several channels are involved. Actually, the later methods have been widely used for the computation of photoassociation rates [19–22], since they can determine very precise energies and wave functions, both for bound and for continuum levels. It has been demonstrated that due to their global character, mapped grid methods are ideally suited to precise computation of the perturbations occurring in molecular spectra, such as Rb<sub>2</sub> [23–25] or K<sub>2</sub> [26] singlet-triplet mixing. In such cases, the perturbation of one level of a given series should be attributed to a large number of bound or continuum levels of the other series, and local perturbation treatments are poorly adapted. However, up to now, attempts to compute the photoassociation line shapes via grid methods have not been very efficient [27,28] and the interpretation of precise measurements is routinely performed with Numerov type approaches [29]. The present paper is proposing an alternative way of implementing grid methods for the calculation of photoassociation line shapes, energy shifts, and rates.

The paper is organized as follows. The description of the present model is reported in Secs. II–IV. The link with previous models, such as the Bohn and Julienne model is discussed in Sec. V, where the various assumptions and approximations are underlined. Application to the cases of sodium photoassociation in the experimental conditions of Ref. [9] is presented in Sec. VI. Section VII will summarize and discuss the outlook of the method.

## II. THE PRESENT MODEL: PRELIMINARY REMARKS

The physical process of photoassociation (PA) can be divided into three steps. *Initially* (step I), a thermal ensemble of cold atoms is in the ground electronic state; the probability to find a colliding pair with relative motion at energy  $E$  and angular momentum  $l$  is given by

$$p_B(E, l) = \frac{(2l+1)\exp[-E/(k_B T)]}{Z_{\text{eq}}}, \quad (1)$$

where  $T$  is the temperature, and  $k_B$  is the Boltzmann constant. The partition function  $Z_{\text{eq}}$  was shown in [30] to be well approximated by the classical expression  $Z_{\text{eq}} = Q_T V = V(2\pi\mu k_B T)^{3/2}/h^3$  for a gas of noninteracting pairs in a volume  $V$ . Further discussion regarding  $Z_{\text{eq}}$  could be found in [30].

The radial wave function which corresponds to the pair is represented with a continuum eigenfunction  $|\psi_{E,l}^g(R)\rangle$  of the single-channel Hamiltonian  $\hat{\mathbf{H}}_{\text{sc}}^{g/e}$ ,

$$\hat{\mathbf{H}}_{\text{sc}}^{g/e} = -\frac{\hbar^2}{2\mu} \frac{d^2}{dR^2} + \frac{l(l+1)}{R^2} + V_{g/e}(R). \quad (2)$$

Here,  $\mu$  is the reduced mass of the pair, and  $V_{g/e}(R)$  is the potential curve for the relevant, here the ground/excited, electronic state.

At the second step (step II), the intensity of a cw laser with frequency  $\omega$  is ramped within a time scale that can be varied from hundreds of ns to several  $\mu\text{s}$ . Along this *preparation* period, the continuum states are coupled to one or more bound vibrational levels  $v, J$  that belong to one or more excited electronic states  $e$ . Each of the levels in the excited state, denoted by  $|\phi_{v,J}^e(R)\rangle$ , may decay spontaneously with a natural free width  $\gamma_{v,J}^{0/e}$ , which is typically at the order of ns. The field that is applied on this stage varies with time, and so are the states of the total system.

Finally, during the stable period of the experiment (step III), the laser reaches its peak constant intensity  $I$ . For the trap-loss or multiphoton detection scheme which will be described here, the duration of this period is on the order of ms.

Each of the energy levels of the system at this step can now be written as

$$|\Psi_j(E)\rangle = \sum_{e,v,J} a_{e,v,J}^j |\phi_{v,J}^e\rangle + \sum_l \int b_j(E') |\psi_{E',l}^g\rangle dE' + \sum_{v',l} c_j |\psi_{v',l}^g\rangle, \quad (3)$$

where we include the possibility of populating bound levels

$|\psi_{v',l}^g\rangle$  of the ground state. In the present work, we shall consider only this third step, which of course is influenced by the preparation step. Since we shall not treat explicitly the preparation step, and possible transitory effects, a rapid switching on of the photoassociation laser will be assumed, justifying sudden approximation. The density of probability for a transition from initial state  $|\psi_{E,i}^g\rangle$  to a final state  $|\Psi_j(E)\rangle$  is given by

$$P_{(E,i)\rightarrow j} = |\langle \Psi_j(E) | \psi_{E,i}^g \rangle|^2. \quad (4)$$

In Sec. IV it will be shown that a knowledge of  $P_{(E,i)\rightarrow j}$  is sufficient to extract the experimental parameters of the PA process. An efficient method to compute the initial and the final states,  $|\psi_{E,i}^g\rangle$  and  $|\Psi_j(E)\rangle$ , is the subject of the next section.

## III. NUMERICAL DESCRIPTION OF THE FIELD-MOLECULE SYSTEM

The initial state is a thermal ensemble composed of atom pairs, with several angular momenta  $l$ . Each pair is coupled to several  $J$  partial waves components on the excited state. For simplicity, the equations will be written hereby for one value  $l$  and  $J$  of the angular momentum. To obtain  $P_{(E)\rightarrow j}$  one has to compute the initial and final eigenstates of the Hamiltonian without and with the light interaction. In the global grid method used here, this is achieved by representation of the Hamiltonian in a certain basis, and then a diagonalization. The diagonalization step is the most expensive computationally, and it scales as  $N^3$  where  $N$  is the number of basis functions. A selection of an appropriate basis prior to the diagonalization is hence crucial for the efficiency of the method.

### A. The initial states: $R$ representation of the unperturbed molecule in a box

Using numerical grid methods, a numerically complete set of eigenvalues and eigenvectors of the time-independent single channel Hamiltonian  $\hat{\mathbf{H}}_{\text{sc}}^{g/e}$  is obtained for the isolated molecule, for the ground and excited potentials. The single channel Hamiltonian in the equally spaced position representation is denoted  $\hat{\mathbf{H}}_{\text{sc}}^R$ . This is achieved by using the mapped Fourier grid method (see, for example, Ref. [15–17,31]). Within the procedure, a unitary transformation  $\hat{\mathbf{U}}_{\text{mapp}}$  is performed on the Hamiltonian Eq. (2), which is written in equally spaced grid  $R$ . The resulted Hamiltonian  $\hat{\mathbf{H}}_{\text{sc}}^x = \hat{\mathbf{U}}_{\text{mapp}}^\dagger \hat{\mathbf{H}}_{\text{sc}}^R \hat{\mathbf{U}}_{\text{mapp}}$  is represented on a grid with nonuniform distribution of points in the position space  $x$ , to take advantage of the phase-space occupancy of the problem. The potential energy operator is written simply as  $\hat{\mathbf{V}}(x)$ , and the kinetic energy operator reads

$$\hat{\mathbf{T}} = -\frac{\pi^2}{2\mu L_x^2} \hat{\mathbf{J}}^{-1/2} \hat{\mathbf{D}} \hat{\mathbf{J}}^{-1} \hat{\mathbf{D}} \hat{\mathbf{J}}^{-1/2}. \quad (5)$$

$L_x$  is the length of the grid,  $\hat{\mathbf{D}}$  is the first derivative operator matrix, given by (assuming even number of grid points)

$$\hat{\mathbf{D}}_{i,j} = \left( \frac{d}{dx} \right)_{i,j} = \begin{cases} 0, & i=j \\ \frac{(-1)^{i-j}}{\sin[(i-j)\pi/N]}, & i \neq j, \end{cases} \quad (6)$$

and  $\hat{\mathbf{J}}(x) = dx/dR$  is the (diagonal) Jacobian operator for the transformation.

A sufficient representation for  $\hat{\mathbf{H}}_{\text{sc}}^R$  by an equally spaced grid demands typically  $N \propto 10^4$  basis functions for the example considered below in Sec. VI. As was shown in [17], the use of a mapped grid leads to a reduction of about an order of magnitude in the basis size, to several thousands.

A diagonalization of  $\hat{\mathbf{H}}_{\text{sc}}^x$  gives the initial, interaction-free, wave functions and their energies for both electronic states  $|\psi_E^g(R)\rangle$  and  $|\phi_{v,j}^e(R)\rangle$ . The eigenvalues with  $E < 0$ , correspond to bound, discrete states and the ones with  $E > 0$  refer to box-normalized quasicontinuum states. The continuum under this picture is therefore tied to the box size from which it was deduced.

In order to take account of the spontaneous emission in the excited channel  $e$ , an imaginary potential is introduced [32]:

$$\hat{\mathbf{V}}_d(R) = i \left( \frac{2}{3c} \right)^3 \frac{|\mu_{eg}(R)|^2 \omega(R)^3}{\hbar}, \quad (7)$$

where  $\mu_{eg}(R)$  is the transition dipole moment, and  $\omega(R) = 2\pi[V_e(R) - V_g(R)]/\hbar$ .

A diagonalization of  $\hat{\mathbf{H}}_{\text{sc}}^x + \hat{\mathbf{V}}_d$  results into complex eigenenergies. The imaginary part of the eigenvalues,  $\gamma_{v,j}^{0e} = \text{Im}(E_{v,j}^e)$  is interpreted as the natural lifetime of the level  $|\phi_{v,j}^e(R)\rangle$ .

## B. The final states

### 1. The field-dressed molecule

A cw laser with constant intensity  $I$ , detuned by  $\Delta_a$  relative to the atomic resonance line, introduces a radiative coupling between the ground state and the excited state. After making the rotating wave approximation, the full dressed Hamiltonian under the interaction can be written as

$$\hat{\mathbf{H}}_R = \begin{bmatrix} \hat{\mathbf{H}}_{\text{sc}}^g & \hat{\mathbf{\Omega}}(R) \\ \hat{\mathbf{\Omega}}(R) & \hat{\mathbf{H}}_{\text{sc}}^e + \Delta_a \end{bmatrix}. \quad (8)$$

The coupling between the ground and the excited state is introduced by the Rabi coupling operator through the transition dipole moment:  $\hat{\mathbf{\Omega}}(R) = -A \hat{\mu}_{eg}(R) \sqrt{I/2c\epsilon_0}$ , where  $\hat{\mu}_{eg}$  is the spatially dependent transition dipole moment between the two electronic states, and  $A$  is an angular factor depending upon the polarization of the laser and the orientation of the molecular axis. In the  $R$  representation  $\hat{\mathbf{\Omega}}(R)$  is a local, i.e., diagonal, operator. A diagonalization of  $\hat{\mathbf{H}}_R$  gives the final states  $|\Psi_j(E)\rangle$ .

### 2. Energy eigenstates representation

For the final states, one has to diagonalize the Hamiltonian describing the interaction of the molecule with the

radiation field routinely for many experimental parameters. A direct diagonalization of  $\hat{\mathbf{H}}_R$  even for the mapped grid representation, is inefficient, mainly due to the redundancy in the representation of the basis for both potentials. An improved representation for the coupled system is hence crucial. This can be obtained by writing  $\hat{\mathbf{H}}_R$  in the energy eigenstates of the single channels Hamiltonians  $\hat{\mathbf{H}}_{\text{sc}}$ . The unitary transformation  $\hat{\mathbf{U}}_{E\text{-rep}}$  is performed on  $\hat{\mathbf{H}}_R$  to give

$$\hat{\mathbf{H}}_{E\text{-rep}} = \hat{\mathbf{U}}_{E\text{-rep}}^\dagger \hat{\mathbf{H}}_R \hat{\mathbf{U}}_{E\text{-rep}}, \quad (9)$$

the Hamiltonian in the energy representation. The eigenvectors that were obtained as the solutions for the single channel problem serve as the transformation matrices between the two representations, so that

$$\hat{\mathbf{U}}_{E\text{-rep}} = \begin{bmatrix} \hat{\mathbf{U}}_{E\text{-rep}}^g & 0 \\ 0 & \hat{\mathbf{U}}_{E\text{-rep}}^e \end{bmatrix}, \quad (10)$$

where  $\hat{\mathbf{U}}_{E\text{-rep}}^{g/e}$  are the matrices which contain the complete set of eigenvectors for the bound and free levels of the ground and excited states,  $|\psi_E^g(R)\rangle$  and  $|\phi_{v,j}^e(R)\rangle$ , respectively.

The coupled channel Hamiltonian in the energy states picture becomes the following.

(a) For the diagonal part in the excited channel subspace

$$\langle \phi_v^e(R) | \hat{\mathbf{H}} | \phi_v^e(R) \rangle = E_v^{0e} + \Delta_a - i\gamma_v^{0e}, E_v^{0e} < 0, \quad (11)$$

where  $\Delta_a$  is the detuning from the atomic resonance, and  $\gamma_v^{0e}$  the natural width for the vibrational level  $e, v$ .

(b) For the diagonal matrix elements in the ground channel subspace:

$$\langle \psi_n^g(R) | \hat{\mathbf{H}} | \psi_n^g(R) \rangle = E_n^{0g}. \quad (12)$$

For clarity, explicit  $l$  and  $J$  dependency is omitted. We remark here again that  $E_n^{0g}$  include both the bound and the quasicontinuum parts of the spectrum.  $E_n^{0g} > 0$  is therefore discrete, for a given box normalization.

(c) For the nondiagonal part of  $\hat{\mathbf{H}}_{E\text{-rep}}$

$$\Omega_{g,n}^{e,v} = \langle \phi_v^e(R) | \hat{\mathbf{H}} | \psi_n^g(R) \rangle. \quad (13)$$

We can employ the  $R$ -centroid approximation for  $\hat{\mu}_{eg}(R)$  and write

$$\Omega_{g,n}^{e,v} = \bar{\Omega} \langle \phi^{e,v} | \psi_n^g \rangle \equiv \bar{\Omega} \mathcal{F}_{g,n}^{e,v}, \quad (14)$$

where now  $\mathcal{F}_{g,n}^{e,v}$  denotes the square root of the Franck-Condon factor between vibrational levels from the two different electronic states.

The advantage of the energy representation is the possibility to pick the energy levels that participate in the process and thus reduce the required basis set. We shall consider formally the case of an isolated resonance where the ground state continuum  $|\psi_n^g(R)\rangle$  is coupled only to single bound level in the excited state  $|\phi_v^e(R)\rangle$ . The detuning from the atomic resonance  $\Delta_a$  could be replaced by  $\Delta$ , the detuning from the excited bound level. A generalization to several bound excited states, or even a whole continuum, is straightforward.

From this point on, we reduce all the indices for the excited state.

By moving to the energy representation we reduce the representation for the coupled channels problem by about one half, to the order of  $N \approx 1000$  in the example discussed below in Sec. VI.

### 3. Getting out of the box: from $E$ to $E'$ representation

Note that so far, the representation of the continuum is done using box unity-normalized wave functions. This box-dependent basis for the continuum is arbitrary, and therefore it could be reduced.

In order to do so, one had to defined a box-independent Franck-Condon factor. Box-independent quantities for the continuum are obtained by moving from the box-normalized to the energy-normalized wave functions. The relation between the two is given by

$$|\tilde{\psi}_n^g(R)\rangle = \left(\frac{\partial E}{\partial n}\right)^{-1/2} |\psi_n^g(R)\rangle, \quad (15)$$

where the inverse of the level density,  $\partial E/\partial n$ , is given simply, for a large enough box, by the energy difference between two adjacent quasicontinuum levels, given under the box-normalization constraint. An energy normalized Franck-Condon profile,

$$\tilde{\mathcal{F}}^v(E) = \sqrt{\frac{\partial E}{\partial n}}^{-1/2} \mathcal{F}_g^{e,n}, \quad (16)$$

could now be obtained.  $\tilde{\mathcal{F}}^v(E)$  is a box-independent, numerically continuous function of the scattering energy. In fact,  $\tilde{\mathcal{F}}^v(E)$  is a physical measure for the energy dependence of the interaction and it is thus the function that one would like to sample for obtaining the minimal energy representation. The alternative basis has to capture the functional energy dependence of the Franck-Condon profile, using the smallest basis. This could be done in principle with any sampling procedure [33]. The technical details regarding the numerical procedure we employed in this work is described in the Appendix.

Assuming such a minimal representation basis was found, we will denote it by  $|g, n'\rangle$  for the ground state continuum, for  $n' > n_B$ ,  $n_B$  being the number of bound states. The expression for the quasicontinuum diagonal part of the full Hamiltonian [Eq. (12)] reads now

$$\langle g, n' | \hat{\mathbf{H}} | g, n' \rangle = E_{n', n'}^{0g}, \quad n' > n_B \quad (17)$$

and all the other diagonal parts remained unchanged. The nondiagonal part in the alternative basis is defined through the energy normalized Franck-Condon profile as

$$\Omega_{g, n'}^e = \bar{\Omega} \tilde{\mathcal{F}}_g^{e, n'} = \bar{\Omega} \sqrt{\frac{\partial E}{\partial n'}} \tilde{\mathcal{F}}^v(E). \quad (18)$$

A diagonalization of the Hamiltonian [Eqs. (17) and (18)] gives the set of eigenstates for the coupled Hamiltonian,  $|\Psi_j(E)\rangle$ , which include components on both channels, with possible contributions from all the bound or free levels. The energy eigenvalues which are obtained are again complex

TABLE I. Summary of the different representations used in this paper.  $N_g$  and  $N_e$  are the typical basis set sizes for the ground and the excited electronic state, respectively, adapted to the example of Sec. VI.

Representation	$N_g$	$N_e$
$R$ : Equally spaced position grid	$10^4$	$10^4$
$x$ : Mapped position grid	$10^3$	$10^3$
$E$ : Energy eigenstates, boxed	$10^3$	$< 10$
$E'$ : Energy eigenstates, nonboxed	$\sim 10^2$	$< 10$

and  $\gamma^j = \text{Im}(E_j)$  is the width of the level  $|\Psi_j(E)\rangle$ . The transition probability from any initially populated state  $|g, n'\rangle$  to any final state  $|\Psi_j(E)\rangle$  is simply

$$P_{(g, n') \rightarrow j} = |\langle \Psi_j(E) | g, n' \rangle|^2. \quad (19)$$

It is important to notice here that because  $|\Psi_j\rangle$  is an eigenstate of the coupled Hamiltonian, a pair that reaches this state at the beginning of the final step of the experiment remains in the same state without any significant dynamics beside an exponential decay with the lifetime  $\gamma^j$ .

Table I summarizes our procedure so far with the different representations and their typical necessary basis sizes. We started from the Hamiltonian on the equally spaced grid representation. A minimal representation of the problem with such a grid demands a basis of about  $N_R = 10^4$  functions. We then used the phase space occupation of the problem to move to a mapped grid, and reduce the basis set in about an order on magnitude to  $N_x = 10^3$ , for each of the electronic states. The transformation to the energy representation reduces the excited state manifold. The reduced  $E'$  representation minimizes the basis for the ground state, so that finally we could solve the whole coupled channels problem with a basis at the order of  $N_{E'} \sim 200$ , or even smaller. At these sizes of basis the method become efficient, even compared to the semianalytic perturbative methods.

In the next section the deduction of the various PA experimental parameters from  $P_{(g, n') \rightarrow j}$  (and  $\gamma^j$ ) is presented.

## IV. EXTRACTION OF THE ENERGY SHIFTS, TRAP-LOSS RATES, AND LINE SHAPES

With the formal definitions of the previous subsection we can now move to define the various physical quantities that are being measured on the system. The probability to find an atom pair with energy  $E_j$  at the beginning of the stable period (which we will denote as zero time) is given by

$$\begin{aligned} p(E_j, 0) &= N_{\text{pair}}(0) \sum_{n'} P_{(g, n') \rightarrow j} p_B(E_{n'}) \\ &= \frac{N_{\text{atom}}^2(0)}{2} \sum_{n'} P_{(g, n') \rightarrow j} p_B(E_{n'}), \end{aligned} \quad (20)$$

where  $N_{\text{atom}}(0)$  and  $N_{\text{pair}}(0)$  are the number of atoms and atom pairs at time 0, and  $p_B$  is defined above [see Eq. (1)]. As was explained at the last paragraph the only dynamics at

the stable period are the exponential decay of the  $j$ th level. At later times thus

$$p(E_j, t) = \exp(-\gamma_j t/\hbar)p(E_j, 0) \quad (21)$$

so that the total probability density for the whole ensemble is

$$\begin{aligned} P_{\text{tot}}(t) &= \sum_j p(E_j, t) \\ &= \frac{N_{\text{atom}}^2(0)}{2} \sum_{n', j} \exp(-\gamma_j t/\hbar) P_{(g, n') \rightarrow j} p_B(E_{n'}). \end{aligned} \quad (22)$$

The observed reaction rate  $v(t)$  at any given time is the change of  $P_{\text{tot}}(t)$  versus time:

$$\begin{aligned} v(t) &= -\frac{dP_{\text{tot}}(t)}{dt} \\ &= \frac{N_{\text{atom}}^2(0)}{2\hbar} \sum_{n', j} \gamma_j \exp(-\gamma_j t/\hbar) P_{(g, n') \rightarrow j} p_B(E_{n'}) \\ &\equiv \frac{N_{\text{atom}}^2(0)}{2\hbar} \langle \gamma(t) \rangle. \end{aligned} \quad (23)$$

The rate could be thus interpreted as the thermally averaged decay. On the other hand, the experimental definition of the diatomic reaction rate for a sample containing  $N_{\text{atoms}}$  is

$$v(t) = K \frac{N_{\text{atoms}}^2(t)}{V}. \quad (24)$$

Now, a comparison between the two expressions yields the relation between the calculated and experimental rate constants, which holds for any given time. Specifically for  $t=0$  one gets

$$K(I, \Delta) = \frac{V \langle \gamma(0) \rangle}{2Z_{\text{eq}}} = \frac{\langle \gamma(0) \rangle}{2Q_T}. \quad (25)$$

In a fashion similar to the experimental, a calculation of  $K$  as a function of the detuning yields the line shape. The peak value of  $K$  as a function of  $\Delta$ , and the value of the detuning at the peak are termed as the maximum reaction rate  $K_{\text{max}}$  and the energy shift  $E_1$  for a given intensity and temperature, respectively.

Before moving forward, we remark that the model is non-perturbative with respect to the laser intensity. It is also well oriented to dynamical, time-dependent-type calculations. Furthermore, a generalization of the method to multiple coupled continuum manifolds, several bound states, or to include hyperfine structure, is straightforward. Its drawback is mainly being a little less efficient computationally, due to the expansive diagonalization step. Nevertheless, this could be overcome, especially for calculating line shapes and saturation effects, as we will show at the application of Sec. VI. But, before doing so, we will present briefly in the next subsection the necessary expressions of the method of Bohn and Julienne [6] (BJ) to which our expression (25) will be compared.

## V. ADJUSTMENT OF BOHN AND JULIENNE MODEL TO THE GRID METHODS FRAMEWORK

In this subsection we present the method of BJ [6], and adjust it to take advantage of the available grid methods. We will limit the treatment to the simple case of a single isolated resonance embedded in a continuum. The scattering-theory-based method defines a scattering amplitude  $S_E$  for a pair of atoms in the center of mass framework. The square of  $S_E$  is referred to as the probability to initiate in a unbound state with kinetic energy  $E$  and be lost at infinite time, due to a light-induced coupling to a bound molecular state.

According to Fano [6,34],  $|S_E|^2$  is given by

$$|S_E|^2 = \frac{\gamma \Omega_E}{(E - \Delta - E_1) - \left(\frac{\gamma + \Omega_E}{2}\right)^2}. \quad (26)$$

Here  $\Delta$  is the detuning of the light frequency of the resonance bound state's energy, and  $\gamma$  is the natural linewidth of the bound level or any other decay due to some lost mechanism.  $E_1$  and  $\Omega_E$  are the energy shift and the stimulated absorption-emission rate, respectively. With the help of second order perturbation theory it was shown in [34] that

$$E_1 = P \int dE' \frac{|\Omega_{E'}|^2}{\Delta - E'}, \quad (27)$$

where  $P$  stands for “the principle part of,” and  $\Omega_E$  is the dipole moment coupling that was defined above [see Eq. (13)].

The rate of loss from the system is given by performing a velocity thermal averaging of  $|S_E|^2$ , for all the initial scattering energies, and with respect to all the relevant partial waves, to obtain the observed rate loss:

$$K = \sum_l \frac{\pi v}{k} \int p_B(E, l) |S_E^l|^2 dE, \quad (28)$$

where the integral over the energy indicates for a thermal averaging over the Boltzmannian distribution  $p_B$ , defined above [see Eq. (1)]. The superscript for  $S$  denotes the rotational quantum number for the partial wave  $l$ , and  $v$  and  $k = \sqrt{2\mu E}/\hbar$  are the relative velocity and the wave number of the atom pair.

It is important to comment here that, in order to calculate the energy dependent  $\Omega_E$  for Eqs. (26)–(28) the energy dependency of the continuum has to be calculated [see Eq. (2)]. The common use of local solvers like the Numerov propagator [33] for that purpose made Fano's formalism impractical computationally. An energy independent  $\Omega_E$  was assumed for demonstrative purposes in Ref. [34]. Obviously, as one can see from Fig. 3 this is far from being adequate to describe molecular systems in any other circumstances.

Using the ideas of Du *et al.* [35] Bohn and Julienne combined the couple of regular and irregular solutions of Eq. (2) to write the energy shift  $E_1$  as

$$E_1 = -2\pi \int_0^\infty r \Omega_E(R) dR \int_0^R i \Omega_E(R') dR', \quad (29)$$

where the superscripts denote the regular and irregular part of the continuum wave function for  $E \rightarrow 0$ , and  $r^i \Omega_E(R)$  is understood to be the integrand of the integral of Eq. (13). As noted in [29,35], this alternative expression could be viewed as a way to write the Green kernel  $\hat{G} = (\hat{H} - E)^{-1}$  in the position representation instead of the energy space used in Fano's formalism.

To reduce even further the effort in the computation of  $\Omega_E$ , the assumption of a slowly varying continuum with respect to  $E$  is employed, i.e.,  $\lim_{E \rightarrow 0} (d\Omega_E/dE) \ll p_B(E \rightarrow 0)$ . Under these conditions, the rate is assumed to be influenced by the on-resonance light interaction.

The continuum is represented now by only a single continuum state and the thermal averaging in Eq. (28) can be avoided. As shown in [36], this leads to

$$K = \frac{h}{2\mu k} \frac{4\gamma\Omega(E_R)}{[\gamma + \Omega(E_R)]^2}, \quad (30)$$

where now the coupling  $\Omega_E$  [defined above in Eq. (13)] is taken only at the resonance energy  $E_R$ .

An analytic alternative way for calculating the energy dependence of  $\Omega$  was suggested in Ref. [37]. In the later work, strong energy dependence, was found in some cases, for instance  $^{85}\text{Rb}$ .

In this paper, we adopt the advantages of the grid methods in the  $E$  representation, and calculate the explicit dependency of  $\Omega(E)$  directly from the continuous energy normalized Franck-Condon profile with any desired accuracy for any energy range. This allows us to calculate  $E_1$  directly using Fano's formalism, without a need to have the irregular solution of the single channel Schrodinger equation. As noted in [29] the two expressions give the same results.

At the next section a comparison between the various expressions will be demonstrated by a concrete application.

## VI. APPLICATION

The example chosen for numerical application will be the on-resonance photoassociation of the  $v=135$ ,  $J=1$  level of  $\text{Na}_2 A^1\Sigma_u^+$  in the experimental conditions of the NIST experiment [9]. The initial state is a pair of colliding atoms with  $l=0$  or 2 (see Fig. 1). The calculations have been performed using the same potentials as in [12]. The position of the repulsive wall in the ground state  $X^1\Sigma_g^+$  has been slightly modified, so that the binding energy of the last levels is  $E(v=65)=0.013 \text{ cm}^{-1}$  for  $l=0$  and  $E(v=64)=0.25 \text{ cm}^{-1}$  for  $l=2$ . The experimental values for these levels are  $E(v=65)=0.013 \text{ cm}^{-1}$  and  $E(v=64)=0.25 \text{ cm}^{-1}$ , respectively. In the excited curve, the level  $v=135$  is bound by  $49.23 \text{ cm}^{-1}$ , the two neighboring levels being  $v=134$  at  $-52.95 \text{ cm}^{-1}$  and  $v=136$  at  $-45.76 \text{ cm}^{-1}$ . Note that in experiment the binding energy of the resonant level is  $43 \text{ cm}^{-1}$ . The natural width is set to  $\gamma=2\pi \times 18.36 \text{ MHz}$  to match the experiment.

Figure 2 presents the coupling profile, i.e., the Franck-Condon factors multiplied by the Rabi frequency [see Eq.

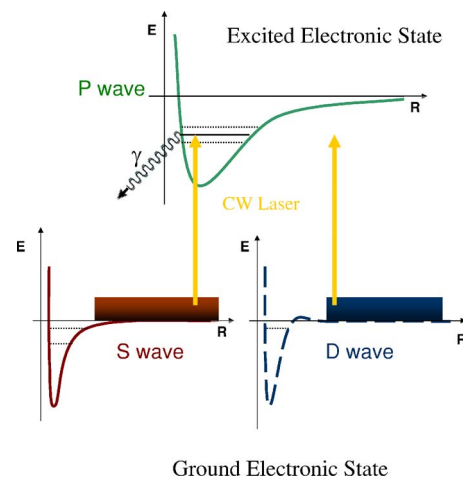


FIG. 1. (Color online) A schematic view of the cw laser PA experiment. Atoms pairs colliding in  $S(l=0)$  and  $D(l=2)$  partial waves on the ground electronic state are coupled by a laser with constant frequency and intensity to the  $v=135$ ,  $P(J=1)$  bound level in the excited electronic state. The nearby bound levels on the excited state, as well as a few bound levels within the ground electronic state, could be coupled as well. The natural lifetime of the bound state  $\gamma = 2\pi \times 18.36 \text{ MHz}$ .

(14), for various bound levels  $v$  of the ground state coupled to one level ( $v=135$ ) of the excited state at intensity of  $1 \text{ W/cm}^2$ . In the main frame  $v$  varies from 0 to 63 and oscillations in the coupling term are visible as the Condon point is moving to large internuclear distances. The FC factors are identical for both partial waves when  $v \leq 63$ . The  $v=65$  level is bound only for the  $S$  wave.

At the upper and the lower panels of Fig. 3 the coupling profile for the continuum part of the spectrum is shown, for

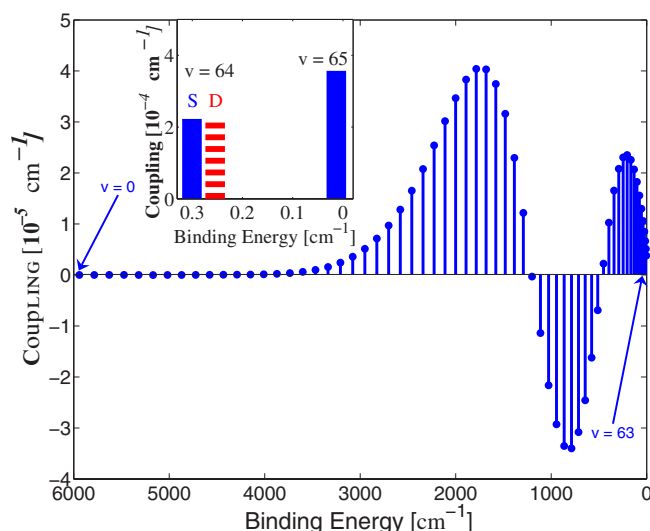


FIG. 2. (Color online) Variation of the coupling term between the level  $v=135$  of  $\text{Na}_2 A^1\Sigma_u^+$  and the vibrational levels of the  $\text{Na}_2$  ground state vs the binding energy. The intensity of the cw laser is  $I=1 \text{ W/cm}^2$ . The rotational quantum number is assumed to be either 0 or 2. The first 64 levels are shown. Inset: The same for the upper levels for a rotational quantum number  $l=0$  (full rectangles,  $v=64$  and  $v_B^0=65$ ) and  $l=2$  (striped rectangle,  $v=v_B^0=64$ ).

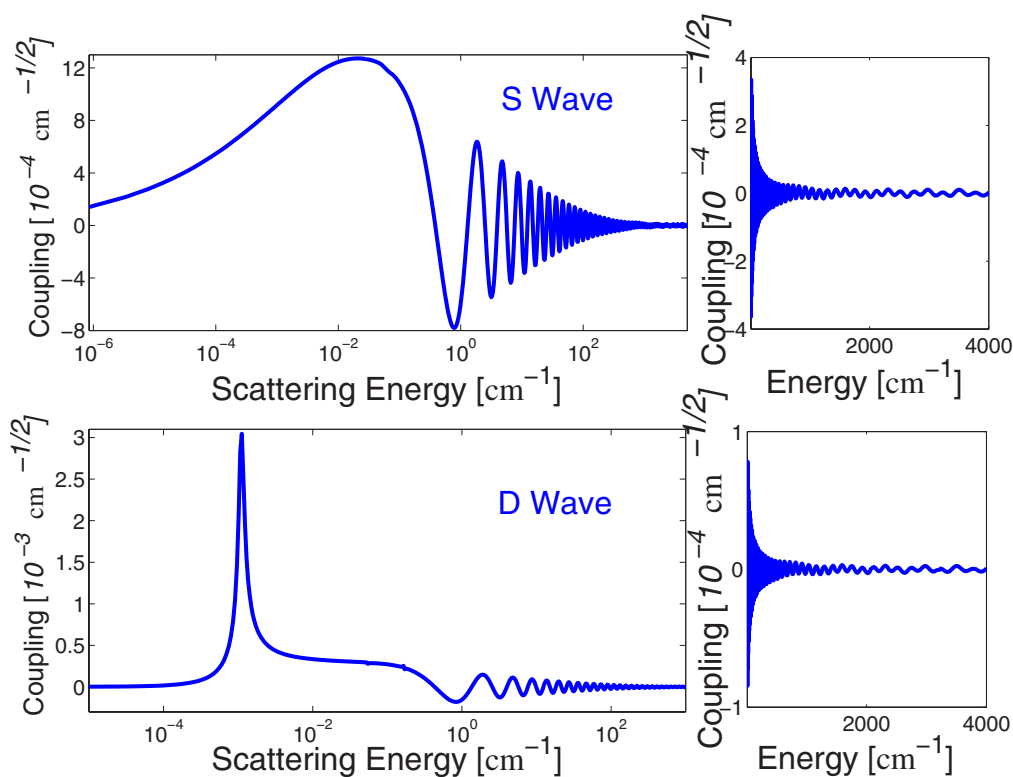


FIG. 3. (Color online) Left: Variation of the coupling term between the level  $v=135$  and the energy normalized  $S$  (upper) and  $D$  (lower) continuum levels of the  $\text{Na}_2$  ground state vs the scattering energy at logarithmic scale. The intensity of the cw laser is  $I=1 \text{ W/cm}^2$ . Right: Same as the left panels, now in a linear horizontal scale.

both  $S$  and  $D$  partial wave, respectively. The left and the right panels show the same profile in logarithmic and linear scale. The last bound level  $n=65$  for the  $S$  wave, is shifted for the  $D$  wave and appears as a shape resonance with a well defined width in the  $D$  continuum. For the continuum part of the spectrum, the Condon point is energy independent. The structure of the coupling profile of the continuum is a signature of the energy dependence of the continuum wave functions [30]. The rotational barrier on the  $D$  potential surface makes the  $D$  profile to vanish more strongly near the threshold than does the  $S$  profile.

In the next subsections the results of grid method will be presented in three steps. First, the light induced energy shift will be calculated and discussed. Then, the results for the rest of the PA observables will be presented in the low intensity regime, where the perturbative method should be adequate. Finally, we present the results for the high intensity regime, where the appearance of saturation effect are explored.

### A. Light induced energy shifts

Using Fano's perturbative expression for the energy shift [Eq. (27)] and the right panels of Fig. 3 it is understood that the energy scale which is needed for the calculation of the energy shift is larger in many orders of magnitude than the thermal energy. (see the Appendix for a numerical example). On the other hand, as will be shown below, the line shape is influenced only by the coupling profile in the vicinity of the thermally populated energy. This separation of scales can

help us furthermore in reducing the basis set, depending upon which physical quantity one would like to calculate.

The light induced energy shifts for intensities up to  $100 \text{ W/cm}^2$  are presented in Fig. 4. They were calculated using the  $S$  continuum part of the ground state manifold. The dotted line is the energy shift that was calculated using the modified Bohn and Julienne perturbative method and is tem-

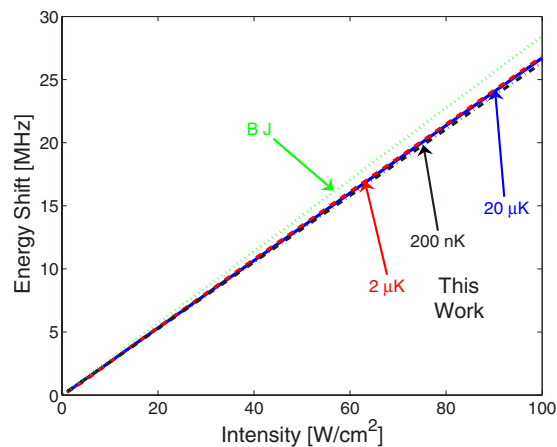


FIG. 4. (Color online) Energy shift as a function of the intensity. The values for the perturbative method are in the dotted line, irrespective on the temperature. In the dashed, solid (barely visible), and dashed-dotted lines: Nonperturbative method, for  $2 \mu\text{K}$ ,  $20 \mu\text{K}$ , and  $200 \text{ nK}$ , respectively. Only the interaction with the  $S$  continuum is considered.

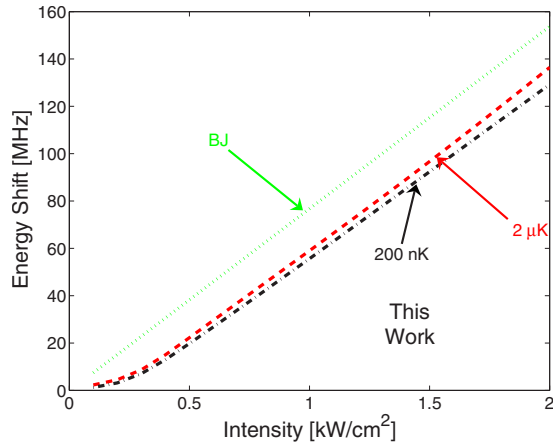


FIG. 5. (Color online) The same as in Fig. 4, with the full interaction:  $S$  and  $D$  continuum manifolds and bound states.

perature independent by definition. In dashed, solid, and dashed-dotted, we present the energy shift using our method for  $T=20$ ,  $2$ ,  $\mu\text{K}$ , and  $200$  nK, respectively. All the curves are linear as expected. A difference exists between the energy shifts, but it is too small to be measurable. The difference in the slopes between the present calculations and the perturbative method is also within the experimental accuracy. An important result we observed in our calculation is that the perturbative linearity of the energy shift with respect to the intensity was conserved for any feasible intensity that was checked (up to  $100$   $\text{kW}/\text{cm}^2$  and higher). Another feature of the perturbative limit is the additivity of the contributions from different partial waves with respect to the bound and the continuum. Figure 5 presents the energy shift for the full interaction, i.e., bound and continuum part of the spectrum for both  $S$  and  $D$  partial waves. No deviations from the perturbative treatment were found with respect to the additivity.

### B. Low intensity regime: Perturbative limit

Saturation effects for the case of photoassociation in a sodium condensate were not observed up to  $1.2$   $\text{kW}/\text{cm}^2$ . A typical line shape for an intensity of  $100$   $\text{W}/\text{cm}^2$ , well below the saturation limit, is presented in Fig. 6. The lines were all centered to zero detuning. The dotted line presents the rate versus the detuning for our method for  $T=500$  nK. In the solid black line the correspondent result for the Bohn and Julienne method with the same temperature is shown. The two lines show the same width but differ at the peak height by less than  $10\%$ , small comparable to the experimental accuracy. Moreover, as can be seen from the dashed line in the figure, a small change of the temperature for the perturbative method (to  $400$  nK) reproduces exactly the same line shape as in our method. Figure 7 presents with the same colors as Fig. 6 the results for the maximum rate  $K_{\text{max}}$  as a function of the intensity. All the curves are linear, as expected for the perturbative regime. Again, the agreement between the two methods is within the experimental accuracy.

We have to remark here that, to our best knowledge, an extensive study of the temperature dependency of photoassociation line shapes has never been performed. Figure 8

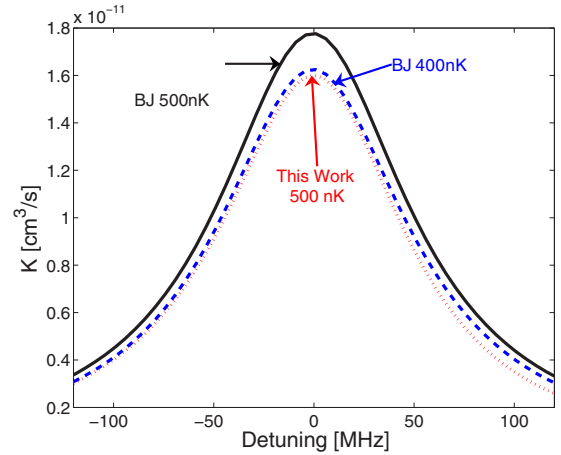


FIG. 6. (Color online) A typical line shape, i.e., rate of loss vs the detuning, for the low intensity regime. (Dotted) The nonperturbative method for  $500$  nK. (Solid and dashed) The perturbative method, for  $500$  nK and  $400$  nK, respectively. All the lines correspond to full energy averaged calculations, and are shifted to be centered at zero detuning, for comparison.

presents the temperature dependency of  $K_{\text{max}}$  for intensity of  $100$   $\text{W}/\text{cm}^2$ . The dashed-dotted and the dotted lines present the values for the thermal averaged rates of expressions (25) and (28). The difference between the methods at the most common temperature for PA experiments in condensates, i.e., a few hundreds of nanokelvins to microkelvins, is at the order the experimental uncertainty. The values deviate significantly from each other at relatively high ( $T > 10$   $\mu\text{K}$ ) and low ( $T < 100$  nK) temperatures. The solid line in Fig. 8 represents the values obtained from the perturbative method without energy averaging [see Eq. (30)]. A single state approximation for the rate seems to be inadequate, at least for the description of most of the temperature dependence of the trap loss. In addition, we checked the results obtained applying the perturbative model (28) with thermal energy averaging but assuming a constant coupling  $\Omega(E)$ . The solid and

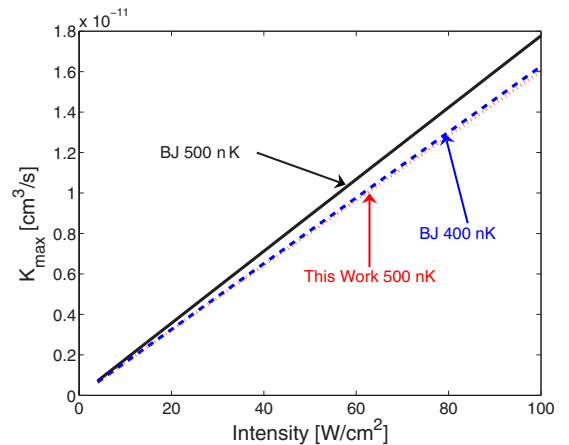


FIG. 7. (Color online) The intensity dependency of the peak loss rate values for a given line shape ( $K_{\text{max}}$ ) for the nonperturbative and perturbative methods. Line shapes are the same as in Fig. 5. All lines correspond to thermally averaged calculation for the assigned temperatures.

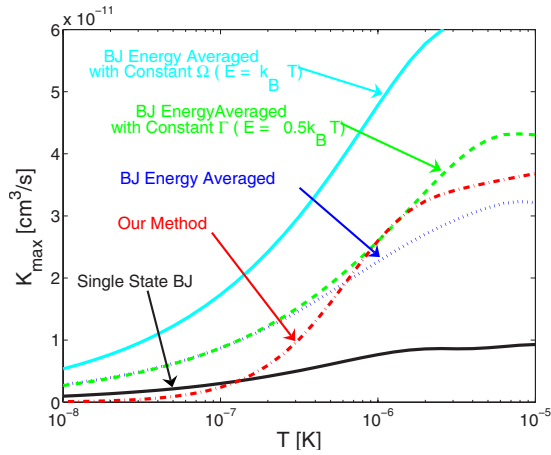


FIG. 8. (Color online) The peak loss rate for a given line shape,  $K_{\max}$ , vs the temperature for the three models. Dashed-dotted: This paper's model. Dotted: Full thermally averaged perturbative. Solid: Single continuum energy approximation; see Eq. (30) in the text. Solid and dashed: Perturbative model with energy averaged but with a constant coupling  $\Omega$ , taken at  $k_B T$  and  $0.5k_B T$ , respectively.

the dashed line show the values for  $\Omega(E=k_B T)$  and  $\Omega(E=k_B T/2)$ , respectively. The constant coupling approximation fits perfectly to the fully thermally averaged model for the low temperature regime with  $E=0.5k_B T$ . Two factors play a role in this situation: The coupling profile (see Fig. 3) and the Boltzmann thermal distribution [see Eq. (1)]. The first increases with  $E$  while the last decreases. From the results it seems that, in our case, the compensation of the two factors takes place at  $E=0.5k_B T$ . Above this temperature, the thermal width starts to play a role, and the constant coupling approximation is no longer valid.

### C. Nonperturbative regime: Saturation effects

We now move to explore the regime of high intensity. In Fig. 9 we present the intensity dependence of  $K_{\max}$  for  $I$  up to

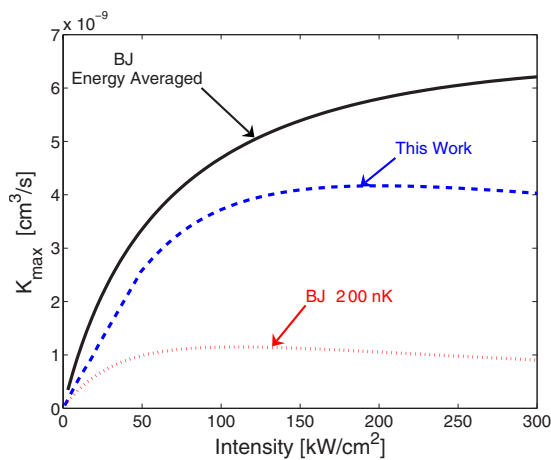


FIG. 9. (Color online) Same as Fig. (7), now for high intensities and  $T=200$  nK, a typical condensate temperature. Dashed and solid are the nonperturbative and the perturbative fully thermally averaged models. Dotted: Single continuum level at 200 nK.

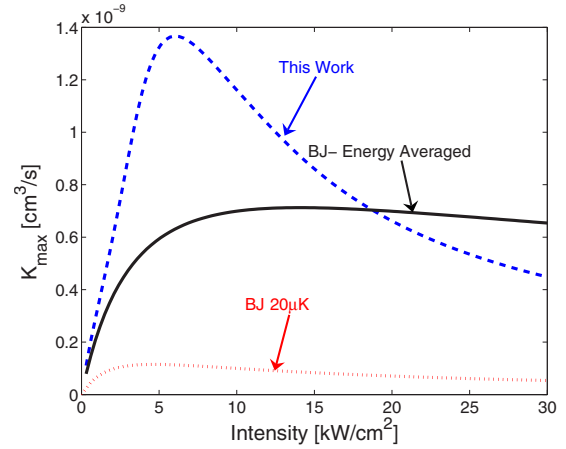


FIG. 10. (Color online) Same as Fig. 9, for  $T=20$   $\mu$ K, a typical temperature for a MOT.

300  $\text{kW}/\text{cm}^2$ . The dashed, solid, and dotted lines are the results for our method, the thermally averaged, and the nonaveraged perturbative method, respectively. The temperature is 200 nK, typical for a condensate. All the lines show saturation behavior, but the saturation limit is not the same. The results for the single energy perturbative approximation are significantly lower than the other two methods. The intensities for reaching saturation are way too high to be observed experimentally and, indeed, were never observed. The validity of the two-body model does not hold for such intensities, and therefore the significance of the results is mainly in predicting a saturation effect for other species where the saturation is reached at lower intensities, e.g., cesium [11], lithium [10], or strontium [38].

Figure 10 presents the same calculations as Fig. 9, but for  $T=20$   $\mu$ K, a typical temperature for a MOT. At a MOT temperature saturation is reached at lower intensities for all the models. The nonperturbative method presents an inverted region in which the peak rate constant decrease with the light intensity. This prediction has never been observed, and it might be feasible experimentally for species other than sodium. The saturation for the case of cesium in a MOT may give a clue to this inverted behavior [11].

A better understanding for the origin of the inverted behavior could be acquired by an inspection of the line shapes near the threshold. Figure 11 exhibits the line shapes computed with the nonperturbative method around the saturation regime. The four lines corresponds to the intensities of 1, 2, 3, and 6  $\text{kW}/\text{cm}^2$  in solid, dotted, dashed, and dotted-dashed, respectively. All the lines are centered to zero detuning for comparison. A shoulder at the positive tail of the Lorentzian line shape starts to develop as saturation is approached. Beyond saturation, the shoulder takes over the Lorentzian line shape at the positive tail of the line to create an unsymmetrical line shape. The power broadening at the negative detuning tail differs from the positive one, and the unsymmetrical form of the line shape is more pronounced with the increase of the intensity. Figure 12 presents the line shapes close to and beyond the saturation limit of the perturbative method, for  $T=20$   $\mu$ K. The lines are centered to zero detuning. Beside the obvious power broadening, the lineshapes remain symmetrical even for high intensities.

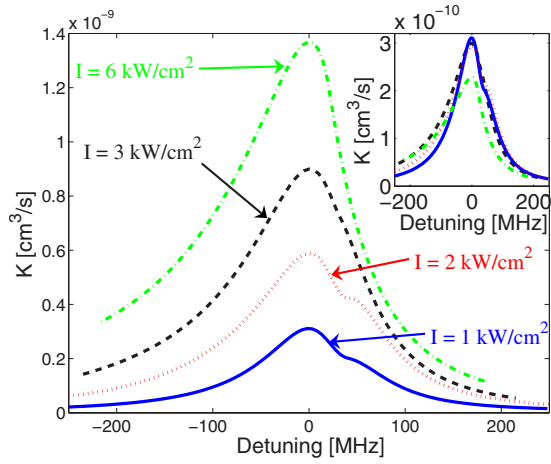


FIG. 11. (Color online) Line shape around the saturation limit, using the nonperturbative method. The temperature is  $T=20 \mu\text{K}$ , and the solid, dashed, dotted, and dashed-dotted lines are for intensities of 1, 2, 3, and 6  $\text{kW}/\text{cm}^2$ , respectively. All the lines are shifted to be centered to zero detuning. For the comparison, the line profiles are normalized to the line of 1  $\text{kW}/\text{cm}^2$ , i.e., the lines for 2, 3, and 6  $\text{kW}/\text{cm}^2$  are divided by 2, 3, and 6.

As a first order perturbative method, the Bohn and Julienne model takes into account only single path processes. That is, the rate constant measures the population flux from the unbound continuum levels to the bound level in the excited state. Any flux that is transferred to the bound level is lost at a rate proportional to the natural linewidth of the bound level. For low temperatures, the thermal energy width is narrow. The loss rate for the off resonance laser is determined only by the detuning from the threshold. Positive and negative detuning are identical in that sense and the line shape is therefore symmetric. For higher temperatures, the population spread is larger and the inner structure of the continuum starts to play a role. This is the origin for the deviation from a Lorentzian line shape which was presented in Fig. 5 of [6], for temperatures of 1 mK. This nonsymmet-

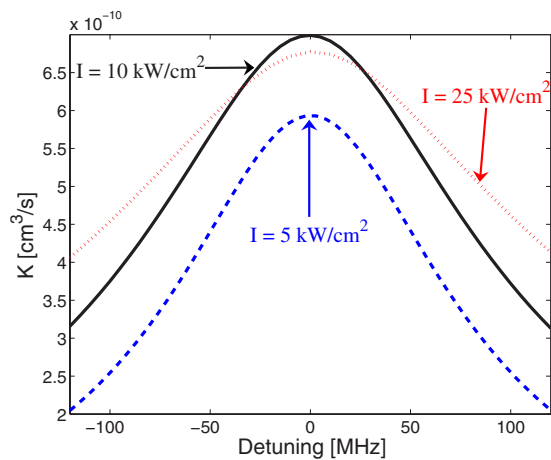


FIG. 12. (Color online) Same as Fig. 11, using the perturbative method. The temperature is  $T=20 \mu\text{K}$ , and dashed, solid, and dotted lines are for intensities of 5, 10, and 25  $\text{kW}/\text{cm}^2$ , respectively. All the lines are shifted to be centered to zero detuning.

TABLE II. Parameters involved in PA and their typical energy scales in kelvins.

Notation	Parameter	Order of magnitude (kelvins)
$E_I$	Energy shifts interaction energy	$10^1 - 10^3$
$\gamma$	Natural linewidth	$10^{-1} - 10^{-3}$
$\Omega_E$	Stimulated emission rate	Depends on $\Delta$ and $I$
$E_T$	Thermal energy	$10^{-7} - 10^{-4}$

ric form is expected to be washed out at low temperatures and high intensities, where the thermal width is much smaller than the radiative width.

In the nonperturbative method, all paths are being taken into account. At large intensity, multipaths processes can take place. A flux could bounce from the bound level back to the continuum and vice versa. Another support for this interpretation could be found in the energy dependence of the transition probability,  $P_{(g,n') \rightarrow j}$ . At low intensity single path processes take place and the transition probability is significant only close to the threshold. At large intensities other parts of the profile play a role,  $P_{(g,n') \rightarrow j}$  deviates from a symmetric Lorentzian and peaks also at the energy of the maximum of the interaction profile. A further increase of the intensity enhances even further the weight of the nonlinear effects on the line shape, and so the line shape at positive detuning is rolled by nonlinear effects. A clue to support this result could be seen maybe at the apparent unsymmetrical line shapes that were measured for the saturation limit of cesium in a MOT (see [11]).

## VII. DISCUSSION AND SUMMARY

In the present paper we have explored the advantage of grid methods for performing a nonperturbative calculation of photoassociation line shapes, energy shifts, and rates. Several physical properties determine the energy scales that are involved in the PA experiment and characterize the outcomes of the various observables. (See Table II.) The energy shift, which is the value of the detuning at which a photoassociation line shape peaks, is the parameter which is the less sensitive to the structure of the interaction profile and the thermal population. In order to calculate it accurately one has to consider an interaction energy which goes up to several hundreds of kelvins and to include all the manifolds which participate in the interaction with the bound level. The interaction energy is independent of the thermal occupation of these levels.

A full nonperturbative treatment for the energy shift is therefore extremely difficult, but fortunately, it is also unnecessary. The advantage of the grid methods in calculating energy shifts is minor and they could be obtained efficiently and accurately by perturbative methods.

For low laser intensities, the natural linewidth of the bound level, which is usually at the order of hundred of MHz, or tens of millikelvin, is the next energy scale in the hierarchy. The width of the line shape and the scaling of the

peak height are determined by this parameter at low intensities. As the intensity of the laser increases, the radiative coupling, or the Rabi frequency of the given scattering energy  $\Omega(E)$  begin to dominate, and lead to power broadening and saturation.

The thermal energy is commonly the smallest energy scale. It ranges from about a hundred of nanokelvins for the coldest condensates, to a few hundreds microkelvins, for “hot” MOTs. For low temperatures, the narrow width of the populated energy band makes the coupling profile to be almost insignificant. Saturation could then be described quite well with the perturbative methods. As the temperature increases, the inner structure of the continuum is encrypted into deviations of the line shape from a symmetric Lorentzian, and an inverted region of the maximum of the rate  $K_{\max}$  as the intensity increases. Some of these deviations, especially the ones which are visible at the low intensity limit, for relatively high temperatures, could be well described by the single-path perturbative models. Other features which result only at high intensities, could be calculated only with the help of the multipath model.

The nonperturbative model that we presented in this paper can serve as a useful tool to model easily other cases where nontrivial line shapes appear. These include the following.

- (a) Photoassociation close to threshold.
- (b) Accidentally degenerate or almost degenerate levels that originate from different electronic states. In both cases, interaction between several levels in the excited state need to be put in the framework of a higher order model. The case of resonant coupling photoassociation [19,20,23,25] is a good example.
- (c) Active interaction between multiple continuum manifolds, where more than a single continuum is populated or depopulated during the process. One possibility is when more than one partial wave participates in the scattering, e.g., the  $D$  resonance in  $^{85}\text{Rb}$  (see [37]). In cases of lower barriers, higher temperatures, or in the cases of processes that take place by explicitly populating the continuum, highly structured line shapes might be resolved by our method.

Finally, the dynamical approach which is the basis for the present study is an important building block for a future comprehensive time dependent description of the many body interaction in the description of PA.

#### ACKNOWLEDGMENTS

This work was supported by the Israel Science Foundation and by the European Commission in the frame of the Cold Molecule Research Network under Contract No. HPRN-CT-2002-00290. The Fritz Haber Center is supported by the Minerva Gesellschaft für die Forschung GmbH München, Germany.

#### APPENDIX

Two purposes are the objects of this appendix: the numerical details of the sampling of the continuum profile  $\tilde{\mathcal{F}}^v(E)$  [see Eq. (16)], and the demonstration of the energy scale that is needed for the calculation of the energy shift.

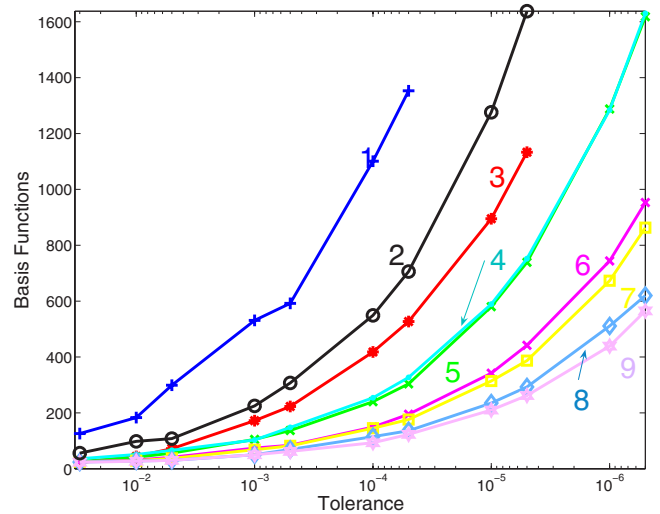


FIG. 13. (Color online) Number of basis function vs the tolerance parameter  $\tau$ . The numbers near the lines stand for different moments of the interaction profile  $\tilde{\mathcal{F}}^v(E)$ . The box normalized from which the original profile is deduced contains 920 basis functions.

The sampling of the continuum profile  $\tilde{\mathcal{F}}^v(E)$  could be done in principle by a global or local numerical sampling procedure (see, for example [33]). The common procedures take advantage of an *a priori* knowledge about the given function to be sampled. In this work we limited ourselves to a naive approach and determined the sampling of the profile *a posteriori* according to the results that were obtained with a given basis. The criterion we employed was the numerical convergence of the integral over a given moment of the interaction profile  $\tilde{\mathcal{F}}^v(E)$ :

$$\mathcal{I} = \int_0^{E_{\text{cut}}} [\mathcal{F}^v(E)]^n dE \approx \sum_j \Delta(E_j) [\mathcal{F}^v(E_j)]^n \quad (\text{A1})$$

where  $n$  is the order of the moment,  $E_j$  is the discrete sampling energy points, and  $\Delta(E_j)$  is the energy difference between two adjacent points. The upper bound for the profile  $E_{\text{cut}}$  is discussed below. The procedure initiates with a small set of points, and a new point is added or rejected between any two old points according to its influence on the value of  $\mathcal{I}$ . The quality of the procedure is determined by the tolerance parameter  $\tau = |\mathcal{I}^{\text{new}}/\mathcal{I}^{\text{old}} - 1|$ . The number of basis functions for sampling the  $S$  continuum, as a function of the tolerance parameter is presented in Fig. 13. The various lines present different moments.

As can be understood, the convergence of the sampling becomes more efficient for higher moments, which emphasize more the features in the profile. Too high moments, however, smear completely the functional structure and so an optimum moment has to be found. We have to comment here that in order to increase the resolution of the basis set with respect to the thermally populated energy near the threshold (for  $E < Nk_B T$ ,  $N$  is usually 10), we inserted a small energy grid (typically 50–100 basis functions) with constant energy step at close-to-threshold energies.

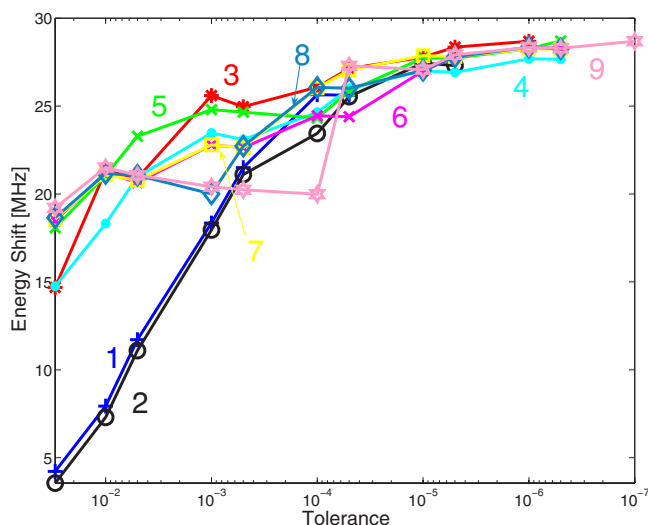


FIG. 14. (Color online) Calculated energy shift vs the tolerance parameter  $\tau$ . The intensity is  $100 \text{ W/cm}^2$ , the temperature is  $2 \mu\text{K}$ . Only calculations with respect to the  $S$  continuum are presented. The continuum is sampled up to an energy of  $300 \text{ K}$ . The numbers near the lines stand for different moments of the interaction profile  $\tilde{\mathcal{F}}^e(E)$ .

In Fig. 14 the resulted energy shifts are plotted as a function of the tolerance parameter for the various moment orders. The numerically exact value which was calculated using the perturbative method is  $27.8 \text{ MHz}$ . The values for moment order above the fifth, convergence to this values within less than 5% for tolerance value of  $5 \times 10^{-5}$ . The basis set that was taken in this paper uses  $\tau=5 \times 10^{-7}$  and  $n=9$ . Larger moments than the chosen exhibit slower convergence and demand much smaller values of  $\tau$  to produce an adequate basis set.

We must remark also that the only physical parameter which demands such care in the sampling is the energy shift.

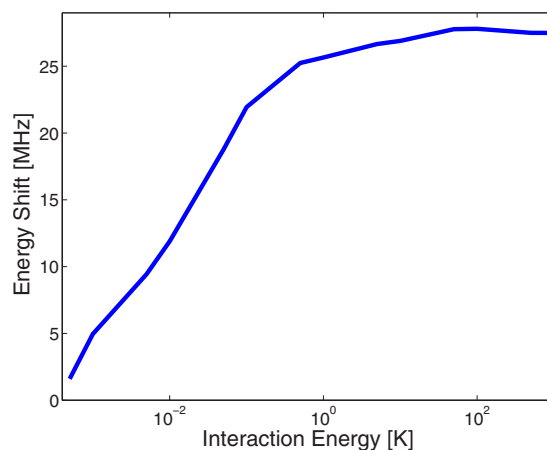


FIG. 15. (Color online) Calculated energy shift vs highest continuum energy to sample. The parameters are identical to Fig. 14. The ninth moment with tolerance of  $5 \times 10^{-7}$  is taken.

The values for the lifetime are much less influenced by the size of the basis, and converged even at  $\tau$  as small as  $1 \times 10^{-3}$ . To demonstrate the importance of very large energy scale that are needed to calculate the energy shift correctly we present in Fig. 15 the calculated energy shift as a function of  $E_{\text{cut}}$ , the upper bound of the energy grid. Convergence of the energy shift is achieved only when reaching hundreds of kelvins. Note, again, that only the energy shift exhibit a sensitivity for such high energies. For low laser intensities the lifetime is found to converge  $E_{\text{cut}}$  at the order of the thermal energy grid. Convergence near the saturation limit demands extension of the grid up to the first minimum of the coupling profile, i.e.,  $10^{-2} \text{ cm}^{-1}$ , or tens of millikelvins. A basis set for such energies contained less than 150 functions and is adequate for calculating most of the line shape features, except for energy shifts.

- 
- [1] H. R. Thorsheim, J. Weiner, and P. S. Julienne, *Phys. Rev. Lett.* **58**, 2420 (1987).
- [2] K. M. Jones, E. Tiesinga, P. D. Lett, and P. S. Julienne, *Rev. Mod. Phys.* **78**, 483 (2006).
- [3] P. Pillet, A. Crubellier, A. Bleton, O. Dulieu, P. Nosbaum, I. Mourachko, and F. Masnou-Seeuws, *J. Phys. B* **30**, 2801 (1997).
- [4] R. Napolitano, *Braz. J. Phys.* **27**, 162 (1997).
- [5] R. Côté and A. Dalgarno, *Phys. Rev. A* **58**, 498 (1998).
- [6] J. L. Bohn and P. S. Julienne, *Phys. Rev. A* **60**, 414 (1999).
- [7] E. Taylor-Juarros, R. Côté, and K. Kirby, *Eur. Phys. J. D* **31**, 213 (2004).
- [8] J. Javanainen and M. Mackie, *Phys. Rev. Lett.* **88**, 090403 (2002).
- [9] C. McKenzie, J. HeckerDenschlag, H. Häffner, A. Browaeys, L. E. E. de Araujo, F. K. Fatemi, K. M. Jones, J. E. Simsarian, D. Cho, A. Simoni, E. Tiesinga, P. S. Julienne, K. Helmerson, P. D. Lett, S. L. Rolston, and W. D. Phillips, *Phys. Rev. Lett.* **88**, 120403 (2002).
- [10] I. D. Prodan, M. Pichler, M. Junker, R. J. Hulet, and J. L. Bohn, *Phys. Rev. Lett.* **91**, 080402 (2003).
- [11] S. D. Kraft, M. Mudrich, M. U. Staudt, J. Lange, O. Dulieu, R. Wester, and M. Weidemüller, *Phys. Rev. A* **71**, 013417 (2005).
- [12] P. Naidon and F. Masnou-Seeuws, *Phys. Rev. A* **73**, 043611 (2006).
- [13] T. Köhler, T. Gasenzer, and K. Burnett, *Phys. Rev. A* **67**, 013601 (2003).
- [14] P. Naidon and F. Masnou-Seeuws, *Phys. Rev. A* **68**, 033612 (2003).
- [15] R. Kosloff, in *Dynamics of Molecules and Chemical Reactions*, edited by R. E. Wyatt and J. Z. Zhang (Dekker, New York 1996), p. 185–230.
- [16] E. Fattal, R. Baer, and R. Kosloff, *Phys. Rev. E* **53**, 1217 (1996).
- [17] V. Kokouline, O. Dulieu, R. Kosloff, and F. Masnou-Seeuws, *J. Chem. Phys.* **110**, 9865 (1999).

- [18] K. Willner, O. Dulieu, and F. Masnou-Seeuws, *J. Chem. Phys.* **120**, 548 (2004).
- [19] C. M. Dion, C. Drag, O. Dulieu, B. Laburthe Tolra, F. Masnou-Seeuws, and P. Pillet, *Phys. Rev. Lett.* **86**, 2253 (2001).
- [20] A. J. Kerman, J. M. Sage, S. Sainis, T. Bergeman, and D. DeMille, *Phys. Rev. Lett.* **92**, 153001 (2004).
- [21] S. Azizi, M. Aymar, and O. Dulieu, *Eur. Phys. J. D* **31**, 195 (2004).
- [22] J. M. Sage, S. Sainis, T. Bergeman, and D. DeMille, *Phys. Rev. Lett.* **94**, 203001 (2005).
- [23] V. Kokoouline, O. Dulieu, and F. Masnou-Seeuws, *Phys. Rev. A* **62**, 022504 (2000).
- [24] V. Kokoouline, O. Dulieu, R. Kosloff, and F. Masnou-Seeuws, *Phys. Rev. A* **62**, 032716 (2000).
- [25] T. Bergeman, J. Qi, D. Wang, Y. Huang, H. K. Pechkis, E. E. Eyler, P. L. Gould, W. C. Stwalley, R. A. Cline, J. D. Miller, and D. J. Heinzen, *J. Phys. B* **39**, S813 (2006).
- [26] C. Lisdat, O. Dulieu, H. Knockel, and E. Tiemann, *Eur. Phys. J. D* **17**, 319 (2001).
- [27] P. Pellegrini, Ph.D. thesis, Université Paris-Sud, Centre d'Orsay, 2003.
- [28] P. Naidon, Ph.D. thesis, Université Pierre et Marie Curie Paris VI, 2004.
- [29] M. Portier, S. Moal, J. Kim, M. Leduc, C. Cohen-Tannoudji, and O. Dulieu, *J. Phys. B* **39**, S881 (2006).
- [30] C. P. Koch, R. Kosloff, E. Luc-Koenig, F. Masnou-Seeuws, and A. Crubellier, *J. Phys. B* **39**, S1017 (2006).
- [31] M. Nest and H.-D. Meyer, *Chem. Phys. Lett.* **352**, 486 (2002).
- [32] F. Laloe, Claude Cohen-Tannoudji, and Bernard Diu, *Mécanique Quantique* (Hermann, Paris, 1973).
- [33] W. H. Press, S. A. Teukolsky, W. T. Vetterling, and B. P. Flannery, *Numerical Recipes*, second ed. (Cambridge University Press, Cambridge, UK, 1995).
- [34] U. Fano, *Phys. Rev.* **124**, 1866 (1961).
- [35] M. L. Du, A. Dalgarno, and M. J. Jamieson, *J. Chem. Phys.* **91**, 2980 (1991).
- [36] J. L. Bohn and P. S. Julienne, *Phys. Rev. A* **60**, 414 (1999).
- [37] A. Crubellier and E. Luc-Koenig, *J. Phys. B* **39**, 1417 (2006).
- [38] S. B. Nagel, P. G. Mickelson, A. D. Saenz, Y. N. Martinez, Y. C. Chen, T. C. Killian, P. Pellegrini, and R. Côté, *Phys. Rev. Lett.* **94**, 083004 (2005).